

Topologically enforced bifurcations in superconducting circuits

Georg Engelhardt, Mónica Benito, Gloria Platero, Tobias Brandes

Angaben zur Veröffentlichung / Publication details:

Engelhardt, Georg, Mónica Benito, Gloria Platero, and Tobias Brandes. 2017.
“Topologically enforced bifurcations in superconducting circuits.” *Physical Review Letters*
118: 197702. <https://doi.org/10.1103/PhysRevLett.118.197702>.



Topologically Enforced Bifurcations in Superconducting Circuits

G. Engelhardt,^{1,*} M. Benito,² G. Platero,² and T. Brandes¹

¹*Institut für Theoretische Physik, Technische Universität Berlin, Hardenbergstrasse 36, 10623 Berlin, Germany*

²*Instituto de Ciencia de Materials de Madrid, CSIC, 28049 Madrid, Spain*

(Received 7 November 2016; published 11 May 2017)

The relationship of topological insulators and superconductors and the field of nonlinear dynamics is widely unexplored. To address this subject, we adopt the linear coupling geometry of the Su-Schrieffer-Heeger model, a paradigmatic example for a topological insulator, and render it nonlinearly in the context of superconducting circuits. As a consequence, the system exhibits topologically enforced bifurcations as a function of the topological control parameter, which finally gives rise to chaotic dynamics, separating phases that exhibit clear topological features.

DOI: 10.1103/PhysRevLett.118.197702

Introduction.—Topological insulators and superconductors have attracted much recent attention. Prominent examples are the integer quantum-Hall effect, chiral edge bands, or topologically protected Majorana fermions [1–3]. These effects are thereby a consequence of a linear, but nontrivial, band structure of noninteracting particles, so that they can also appear in bosonic and even classical systems [4–12].

However, in actual physical systems nonlinearities are omnipresent, whether or not they are desired. They give rise to outstanding and various effects as bifurcations, synchronization, and chaos appearing in different kinds of fields reaching from cold atoms, biology, and chemistry to superconducting circuits [13–16]. For this reason it is interesting to explore the relationship of nonlinear dynamics and linear topological effects.

One of the simplest models exhibiting topological effects is the celebrated Su-Schrieffer-Heeger (SSH) model [17,18], which features topologically protected boundary excitation due to its coupling geometry, as sketched in Fig. 1(a). Thereby, the topological effects can be explained using linear algebra.

In this Letter, we demonstrate that the nonlinearly rendered SSH model proposed in a superconducting circuit [Fig. 1(b)] exhibits topologically enforced bifurcations that lead to chaotic dynamics. This effect is robust and does not depend on system details. Our analysis is based on an effective coupling potential and refers to the number of fixed points of two specific topologically distinct limiting cases, which are depicted in Figs. 1(e) and 1(f). Although referring here to a very specific model, our findings are relevant for all kind of lattice models with possible topological coupling geometry, where nonlinearities are so strong that bifurcations can occur, as in cold-atomic systems [19–21], optomechanics [22], or optics with nonlinear materials [23–25].

In the literature, the effects of nonlinearities due to interactions are mostly considered in the context of ground-state properties of topological systems [26]. Another well-known subject is fractional excitations close to the ground

state [27–30]. Very recently, topological phase transitions induced by a combination of driving and nonlinearities have been investigated [31]. Here, we follow a different approach by investigating the complex nonlinear dynamics, for which, in principal, the total phase space is relevant.

System.—We consider a one-dimensional system of N nonlinearly coupled nodes, as sketched in Figs. 1(a) and 1(b). The equations of motion (EOM) determining the dynamics read

$$\ddot{\phi}_n = t_{n-1,n} f \delta(\phi_{n-1} - \phi_n) + t_{n,n+1} f \delta(\phi_{n+1} - \phi_n) - \mathcal{R} \dot{\phi}_n + I_{ac} \cos(\Omega t), \quad (1)$$

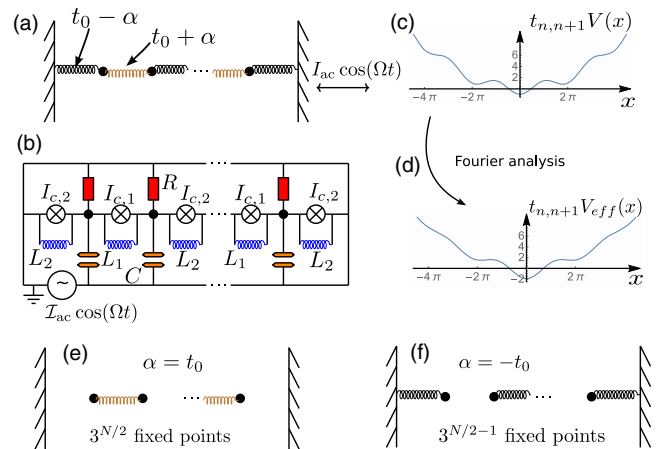


FIG. 1. (a) Sketch of the system. The coupling geometry resembles the one of the SSH model with alternating coupling strength. The system is subjected to external driving and dissipation (nonsketched). (b) Superconducting circuit giving rise to Eq. (1). (c) Nonlinear coupling potential of the nodes. (d) Effective coupling potential appearing due to a Fourier analysis of Eq. (1). (e) Topologically trivial limiting case $\alpha = t_0$, where the system consists of uncoupled dimers. (f) Topologically nontrivial limiting case $\alpha = -t_0$, where two uncoupled nodes at the boundary exist.

where the nonlinearity enters via the function

$$f_\delta(x) = (1 - \delta)x + \delta \sin(x). \quad (2)$$

These EOM can be modeled by a system of superconducting islands coupled by inductively shunted Josephson junctions, as sketched in Fig. 1(b) [32–37]. Thereby, the variables ϕ_n describing the dynamics of the superconducting islands are the node fluxes [32,38], which here are the time-integrated voltages with respect to the ground $\phi_n(t) = (\hbar/2e) \int_{-\infty}^t dt V_n(t)$. Superconducting circuits allow for a large variety of realizations and a broad range of possible parameters [33–36]. We assume large $C\hbar I_{c,n}/e^2 \gg 1$ and $h/4e^2 R \gg 1$, where C , $I_{c,n}$, and R denote capacitance, critical Josephson current, and resistance, as depicted in Fig. 1(b). This parameter regime justifies treating $\phi_n(t)$ as classical variables [34]. The strength of the nonlinearity can be adjusted by δ [33]. Additionally, the dynamics is subjected to a monochromatic driving with amplitude I_{ac} and frequency Ω . It is straightforward to derive the EOM Eq. (1) using Kirchhoff's first law and find the relation of the physical parameters R , C , $I_{c,n}$, and L_n and the parameters appearing in Eq. (1) [32,38].

The position-dependent couplings possess an alternating structure and read

$$t_{n,n+1} = t_0 - \alpha(-1)^n, \quad (3)$$

where 2α is the difference of two subsequent couplings. Thus, the system exhibits the same coupling geometry as the SSH model [17].

The EOM are designed in such a way that, in the linear case $\delta = 0$, the spectrum of the modes reproduces the properties of the standard SSH model, which exhibits a topological phase transition at $\alpha = 0$ [39]. Thereby, the system has topologically protected boundary modes with frequency $\omega_b = \sqrt{2}t_0$ in the topologically nontrivial phase for $\alpha < 0$, which are absent in the topologically trivial phase for $\alpha > 0$. As we see later, features of the linear SSH model still persist in the chaotic dynamics of the nonlinear model.

Time evolution.—In Figs. 2(a) and 2(b) we depict the time evolution of node $n = 1$ for $\delta = 0$ and $\delta = 0.95$, respectively. Throughout the Letter, we choose to drive with a frequency $\Omega = \omega_b$ corresponding to the topologically protected boundary mode appearing for $\delta = 0$ and $\alpha < 0$ to elucidate the topological effects. Instead of depicting the node fluxes $\phi_n(t)$, we consider

$$I_n(t) = \dot{\phi}_n(t). \quad (4)$$

This quantity is proportional to the current flowing from node n through the resistance R to the ground and is therefore experimentally accessible [34]. Additionally, we find that I_n instead of ϕ_n is more appropriate for our investigation, as slow contributions in ϕ_n have a smaller weight.

We always choose $\phi_n(t=0) = \dot{\phi}_n(t=0) = 0$ as the initial state. In Figs. 2(a) and 2(b) we show the time

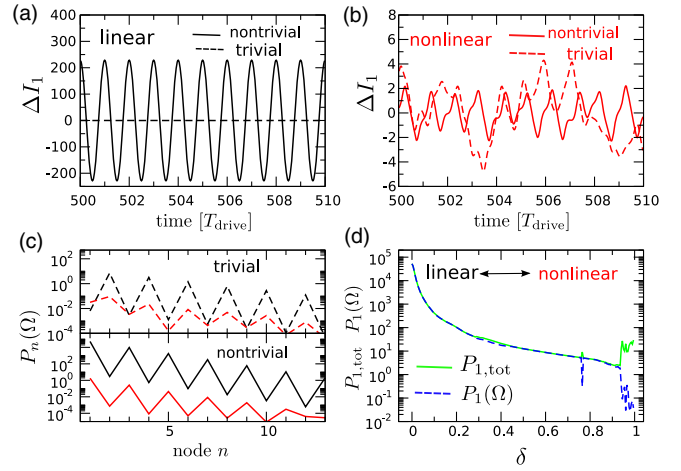


FIG. 2. (a) Current $\Delta I_1 = I_1(t) - I_{\text{bulk}}(t)$ in units of t_0/R flowing from node $n = 1$ through the resistance R to the ground in the linear system $\delta = 0$. Parameters are $\alpha = -0.4t_0$ (nontrivial, solid line) and $\alpha = 0.2t_0$ (trivial, dashed line), $\mathcal{R} = 0.02t_0\Omega$, $I_{ac} = 4t_0$, and $N = 200$. $T_{\text{drive}} = 2\pi/\Omega$ denotes the driving period, where $\Omega = \sqrt{2}t_0$. (b) As in (a) but for $\delta = 0.95$. In this case, the system exhibits chaos. (c) $P_n(\Omega)$ in units of $(t_0/\mathcal{R})^2$ in Eq. (5) for the time evolutions in (a) and (b). Throughout this Letter, we take $t_{\text{min}} = 500T_{\text{drive}}$ and $\tau = 100T_{\text{drive}}$ to evaluate Eq. (5). (d) Dependence of $P_1(\Omega)$ and $P_{1,\text{tot}}$ in Eq. (6) as a function of δ .

evolution after an initial transient phase in order to make sure that we have approached the corresponding attractor. To obtain a clearer understanding, we depict the difference $\Delta I_n(t) = I_n(t) - I_{\text{bulk}}(t)$, where $I_{\text{bulk}}(t)$ denotes the bulk current. This is the time-periodic current under a periodic boundary condition $\phi_{N+1} = \phi_n$ and reads $I_{\text{bulk}}(t) = \text{Im}[\phi_0 \Omega e^{i\Omega t}]$, with $\phi_0 = I_{ac}/\Omega(i\mathcal{R} - \Omega)$ [32].

For the parameters in Fig. 2(a), the time evolution exhibits a harmonic oscillation. Because of the subtraction of the bulk current, the oscillation at node $n = 1$ for $\alpha = 0.2$ (trivial phase) vanishes nearly completely, while the oscillation amplitude is extremely large for $\alpha = -0.4$ (nontrivial phase). To further analyze this dynamic, we consider the position-dependent power spectral density [16]:

$$P_n(\omega) = |\tilde{I}_n(\omega)|^2, \quad (5)$$

$$\text{with } \tilde{I}_n(\omega) = \lim_{\tau \rightarrow \infty} \frac{2}{\tau} \int_{t_{\text{min}}}^{t_{\text{min}}+\tau} dt [I_n(t) - I_{\text{bulk}}(t)] e^{i\omega t}.$$

For long times, the dynamics of the linear system displays harmonic oscillations with frequency Ω of the external driving. For this reason, we depict $P_n(\Omega)$ in Fig. 2(c). Here we observe an alternating pattern of finite and almost zero power as a function of n . Thereby, the power is finite on odd (even) nodes in the nontrivial (trivial) phase. This is a typical topological feature of the linear model [18,32] and a consequence of the chiral symmetry of the SSH model. In Eq. (1) for $\delta = 0$ and small \mathcal{R} this means that the steady state $\phi_n(t)$ becomes $\phi_n(-1)^n$ or $\phi_n(-1)^{n+1}$ when changing the driving frequency as $\Omega \rightarrow \sqrt{4t_0 - \Omega^2}$. As the steady

state for $\Omega = \sqrt{2t_0}$ is unique, the oscillations vanish on either the even or odd nodes.

For a finite δ , the system can exhibit a chaotic time evolution, as depicted in Fig. 2(b). Surprisingly, despite the chaotic dynamics, the power spectral density still exhibits an alternating structure. Note that the overall power is considerably smaller than in the linear case. This is a consequence of the nonlinearity, which we investigate in Fig. 2(d), where we depict $P_1(\Omega)$ and the position-resolved total power,

$$P_{n,\text{tot}} \equiv \int_0^\infty d\omega P_n(\omega), \quad (6)$$

for $n = 1$ as a function of δ . We observe that, starting from $\delta = 0$, the power rapidly decreases. This happens as the driving frequency Ω is no longer in resonance with the boundary mode of the linear system, which is modified due to the nonlinearity δ . For $\delta = 0$, $P_{n,\text{tot}}$ and $P_n(\Omega)$ coincide, as the time evolution is harmonic with frequency Ω . This situation can be observed for a broad range of δ values. In a region around $\delta \approx 1$, both quantities strongly deviate and we find chaos. We are interested in this region, so we concentrate on $\delta = 0.95$ in the remainder of this Letter.

Order parameter.—A useful quantity that gives insight into the dynamics of the system is given by

$$\chi = \frac{P_1(\Omega) + P_2(\Omega)}{P_{1,\text{tot}} + P_{2,\text{tot}}}, \quad (7)$$

which we introduce as an order parameter for the phase diagram in Fig. 3(a). There we depict χ as a function of α and I_{ac} , where we observe several regions among which we find periodic and chaotic dynamics. If the system synchronizes with the external driving, then $P_{n,\text{tot}} \approx P_n(\Omega)$ and $\chi = 1$. On the contrary, for chaotic dynamics, the power distributes over many modes, so that $\chi \approx 0$, as can be seen in Fig. 2(d) for $\delta \approx 1$. Instead of defining $P_1(\Omega)/P_{1,\text{tot}}$ as an order parameter, we choose to incorporate the power of $n = 2$ in Eq. (7). In doing so, we avoid a division by very small $P_{1,\text{tot}}$ appearing, e.g., for $\alpha \gg 0$. The regions marked by A exhibit periodic dynamics, while in B_1 we observe quasiperiodic dynamics. In the regions labeled by B_2 and C we find chaotic time evolutions. We also calculated the power spectrum and the Lyapunov exponent (not shown) to verify that the dynamics is indeed chaotic.

Topological character.—The chaotic dynamics in regions B_2 and C is qualitatively different. To see this, we consider the following quantity:

$$\Delta = \frac{P_1(\Omega) - P_2(\Omega)}{P_1(\Omega) + P_2(\Omega)}. \quad (8)$$

In the linear system, $\Delta = 1$ and $\Delta = -1$ in the nontrivial and trivial phase, respectively [compare with Fig. 2(c)], which is a consequence of the chiral symmetry. In Fig. 3(b), we investigate how this quantity is modified in the nonlinear system $\delta = 0.95$ for increasing driving amplitude I_{ac} . For small driving I_{ac} , the time evolutions corresponds to the

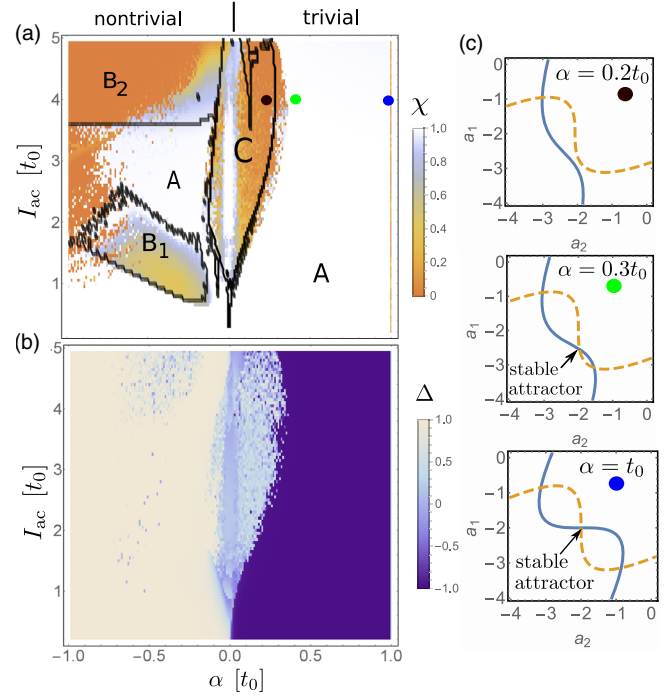


FIG. 3. (a) Phase diagram for the order parameter χ defined in Eq. (7). Parameters are as in Fig. 2. Black lines depict the phase boundary obtained by the generalized force functionals Eq. (10). (b) Phase diagram of the topological order parameter Δ . (c) Level sets $G_1 = 0$ (solid line) and $G_2 = 0$ (dashed line) of Eq. (10) for fixed, but optimized a_3 for $I_{\text{ac}} = 4t_0$. The corresponding parameters are marked in (a) by colored dots. The vanishing of the stable attractor at $\alpha \approx 0.25t_0$ triggers the chaotic dynamics observed in the central region of the phase diagram.

one of the linear model $\delta = 0$. In this case, we observe a fast crossover from $\Delta = 1$ to $\Delta = -1$ at $\alpha \approx 0$.

It is very surprising to see that there is a clear topological character Δ in wide parts of the phase diagram. Even more appealing is the observation that region C can be clearly recognized in Fig. 3(b), while region B_2 cannot. More precisely, the underlying topology in B_2 is more strongly pronounced than in C. Even for chaotic dynamics the oscillations tend to synchronize for nodes within the bulk. As $\phi_n - \phi_{n+1}$ is small, linearization restores chiral symmetry there explaining the alternating power in Fig. 2(c). Remarkably, even for $n = 1, 2$ this alternation is apparent although the chiral symmetry is only fulfilled in the linear order of $\phi_1 - \phi_2$. As we show below, there is also a different mechanism behind the appearance of chaos in regions C and B_2 [Fig. 3(a)].

Time-independent effective equations.—To gain more insight, we derive time-independent nonlinear equations that capture the underlying processes. We observe that the time evolution of ϕ_n in the regular regimes $\chi \approx 1$ is essentially given by a harmonic oscillation up to a small correction $\Delta_n(t)$. Accordingly, we split the time evolution as [40]

$$\phi_n(t) = a_n \cos(\Omega t) + \Delta_n(t). \quad (9)$$

The dynamics in zeroth order of Δ_n is thus determined by the amplitudes a_n . After inserting ansatz Eq. (9) into the EOM Eq. (1), we perform a Fourier analysis. In doing so, we obtain a set of nonlinear equations [32],

$$0 = t_{n-1,n}F_\delta(a_{n-1} - a_n) + t_{n,n+1}F_\delta(a_{n+1} - a_n) + I_{ac} + \Omega^2 a_n \equiv G_n[\{a_n\}], \quad (10)$$

with

$$F_\delta(x) = (1 - \delta)x + 2\delta\mathcal{J}_1(x) \equiv \frac{d}{dx}V_{\text{eff}}(x), \quad (11)$$

which determine the amplitudes a_n . Here, $\mathcal{J}_1(x)$ denotes the first-order Bessel function. The G_n can be considered as generalized force functionals in Fourier space and $V_{\text{eff}}(x)$ as an effective coupling potential. The latter is depicted in Fig. 1(d). In the derivation, we have neglected the dissipative term, as \mathcal{R} is small. A linear stability analysis for Δ_n reveals the stability of the amplitudes a_n . In order to distinguish phases B_2 and C , we numerically minimize

$$\mathcal{G} = \sum_n G_n^2,$$

instead of finding a root of $G_n = 0$ and check whether or not the minimum of \mathcal{G} is a root of Eq. (10). As \mathcal{G} exhibits a large number of minima, it is important to find the one corresponding to the actual steady-state dynamics. In the numerical minimization, we choose a starting point that resembles the amplitudes a_n of the steady state of the linear system, up to a normalization [32]. We find that our approach reproduces the actual dynamics with high accuracy where $\chi \approx 1$.

Fixed-point analysis.—The outcome of the fixed-point analysis of Eq. (10) is included in Fig. 3(a), shown by black lines. Thereby, we distinguish three cases. First, the minimum of \mathcal{G} discovered by the numerics is a root of Eq. (10) and is stable in the linear stability analysis (region A). Second, we discover a root, but it is linearly unstable (region B). Third, the minimum of \mathcal{G} is not a root of Eq. (10) (region C). The most interesting case is the latter as, according to the following fixed-point analysis, it has a topological origin. To understand this, we first investigate the limiting cases $\alpha = \pm t_0$ in more detail.

For $\alpha = t_0$, the system consists of $N/2$ decoupled dimers, as sketched in Fig. 1(e). We depict the level sets of $G_1 = 0$ and $G_2 = 0$ in Fig. 3(c). We observe a symmetric pair of lines which intersect three times; thus, there are three distinct fixed points, where only the middle one is a stable attractor. Altogether, the chain thus exhibits $3^{N/2}$ fixed points for $\alpha = t_0$.

In the case $\alpha = -t_0$, we have $N/2 - 1$ decoupled dimers and two isolated nodes at the ends of the chain, as sketched in Fig. 1(f). The function G_1 does not depend on a_2 . In this case, G_1 has only one root (this is also true for G_N). Altogether, the chain has $3^{N/2-1}$ fixed points. Thus, there is a different number of fixed points in the limiting cases $\alpha = \pm t_0$. Consequently, when varying α from one limiting case to the other one, there are topologically enforced bifurcations.

In particular, as the stable fixed points of the limiting cases $\alpha = \pm t_0$ are structurally different, there is no way to smoothly transform one into the other without bifurcation.

To illustrate this, we included in Fig. 3(c) illustrations for $\alpha = 0.2t_0$ and $\alpha = 0.3t_0$. Thereby, we insert a_3 found by the numerical minimization of \mathcal{G} into the equation for G_2 as a fix parameter. These two panels depict the situation shortly before and after the bifurcation. This bifurcation is a so-called saddle-node bifurcation, where two fixed points annihilate each other by varying α [15].

The middle fixed point corresponds to a stable attractor of the system. When we lower α , the stable attractor vanishes in a bifurcation, and the unstable fixed point remains ($\alpha = 0.2t_0$). Consequently, there is no stable periodic attractor, so that the dynamics gets chaotic. By further decreasing α , the remaining root can either become stable so we enter again in a periodic regime or it stays unstable, which finally results in the chaotic phase B_2 . The appearance of chaotic dynamics usually depends on many parameters, e.g., the minute ratio of driving frequency and driving amplitude. We emphasize that here the chaos is a consequence of the unavoidable topologically enforced bifurcations and therefore is robust.

Discussion.—Our investigations reveal interesting effects appearing in the nonlinearly rendered SSH model. The time evolution exhibits periodic dynamics, quasiperiodicity, and even chaos.

Despite the similarity of the periodic dynamics of the linear and nonlinear EOM, the nonlinear dynamics exhibits a rich fixed-point structure in contrast to the linear system, where there is only one fixed point. The parametric dependence of the fixed points enforces bifurcations, which give rise to a chaotic regime, separating the two areas with distinct topological character $\Delta = \pm 1$. Comparing the structure of the fixed points of the two topological limiting cases, we found that it is not possible to smoothly transform one into the other without a bifurcation. Thereby, the previously stable fixed point vanishes, which gives rise to chaos. This is in strong analogy to the topology of the linear system, where the presence and absence of topologically protected boundary modes is also apparent from a consideration of the topological limiting cases. Despite this analogy, it is not possible to apply the topological concepts known from the linear model, namely, the winding number [18], to describe the topologically enforced bifurcations, which refers to a fixed-point analysis. Nevertheless, the topologically enforced bifurcation and the topological phase transition of the linear model are both independent of the system size due to the previously mentioned arguments, which we confirmed by simulating smaller system sizes (not shown). For instance, for 20 nodes the phase diagram in Fig. 3(a) exhibits larger chaotic regions in the nontrivial part $\alpha < 0$. We also mention that the topologically induced chaos is reminiscent of the topological instability appearing at the phase transition considered in Ref. [10], although the underlying reason is different. By introducing the order

parameter Δ quantifying the topological character of the dynamics, we found that there are two types of chaotic dynamics, only one of which is indicated clearly by Δ . In the other chaotic region, the time evolution surprisingly still exhibits the topological features of the linear model. We emphasize that the order parameters Δ and χ are experimentally accessible by measuring the current of the first two nodes $n = 1, 2$ only. This could be possible with similar experimental techniques as those in Refs. [33–37,41]. Finally, we emphasize that, due to their topological origin, our findings do not depend on details of the system. The topological-enforced bifurcations appear also, e.g., with a different kind of dissipation or for $\delta = 1$. The latter case is particularly important as such types of Josephson junction arrays are used to fix the voltage standard [42]. So this type of setup could also be used to test our findings. Furthermore, the form of the nonlinearity is not relevant. Bifurcations occur even for, e.g., a $-x^3$ term in Eq. (2) instead of the sine, which also suggests that our findings can appear in other types of systems. We also suppose that the effects discussed here appear in more complex systems with underlying nontrivial topology, such as nonlinear versions of the two-dimensional Hofstadter or Haldane models [43,44].

The authors gratefully acknowledge financial support from the DFG Grants No. BR 1528/7, No. BR 1528/8, No. BR 1528/9, No. SFB 910, and No. GRK 1558, as well as inspiring discussion with Jordi Picó, Jan Tötz, and Anna Zakharova. This work was supported by the Spanish Ministry through Grant No. MAT2014-58241-P and the FPI program.

*georg@itp.tu-berlin.de

- [1] D. J. Thouless, M. Kohmoto, M. P. Nightingale, and M. den Nijs, *Phys. Rev. Lett.* **49**, 405 (1982).
- [2] M. Z. Hasan and C. L. Kane, *Rev. Mod. Phys.* **82**, 3045 (2010).
- [3] B. A. Bernevig and T. L. Hughes, *Topological Insulators and Topological Superconductors* (Princeton University Press, Princeton, NJ, 2013).
- [4] R. Süssstrunk and S. D. Huber, *Science* **349**, 47 (2015).
- [5] M. C. Rechtsman, J. M. Zeuner, Y. Plotnik, Y. Lumer, D. Podolsky, F. Dreisow, S. Nolte, M. Segev, and A. Szameit, *Nature (London)* **496**, 196 (2013).
- [6] M. Hafezi, S. Mittal, J. Fan, A. Migdall, and J. Taylor, *Nat. Photonics* **7**, 1001 (2013).
- [7] S. McHugh, *Phys. Rev. Applied* **6**, 014008 (2016).
- [8] G. Engelhardt and T. Brandes, *Phys. Rev. A* **91**, 053621 (2015).
- [9] V. Peano, M. Houde, C. Brendel, F. Marquardt, and A. A. Clerk, *Nat. Commun.* **7**, 10779 (2016).
- [10] G. Engelhardt, M. Benito, G. Platero, and T. Brandes, *Phys. Rev. Lett.* **117**, 045302 (2016).
- [11] V. Peano, M. Houde, F. Marquardt, and A. A. Clerk, *Phys. Rev. X* **6**, 041026 (2016).
- [12] C. H. Lee, G. Li, G. Jin, Y. Liu, and X. Zhang, *arXiv:1701.03385*.
- [13] J. Tomkovič *et al.*, *arXiv:1509.01809*.
- [14] K. Baumann, C. Guerlin, F. Brennecke, and T. Esslinger, *Nature (London)* **464**, 1301 (2010).
- [15] S. H. Strogatz, *Nonlinear Dynamics and Chaos: With Applications to Physics, Biology, Chemistry, and Engineering* (Westview Press, Boulder, 2014).
- [16] R. Kautz, *Rep. Prog. Phys.* **59**, 935 (1996).
- [17] W. P. Su, J. R. Schrieffer, and A. J. Heeger, *Phys. Rev. Lett.* **42**, 1698 (1979).
- [18] J. K. Asbóth, L. Oroszlány, and A. Pályi, in *A Short Course on Topological Insulators*, Lecture Notes in Physics Vol. 919 (Springer, Berlin, 2016).
- [19] N. Goldman, J. Budich, and P. Zoller, *Nat. Phys.* **12**, 639 (2016).
- [20] O. Morsch and M. Oberthaler, *Rev. Mod. Phys.* **78**, 179 (2006).
- [21] M. Aidelsburger, M. Atala, M. Lohse, J. T. Barreiro, B. Paredes, and I. Bloch, *Phys. Rev. Lett.* **111**, 185301 (2013).
- [22] T. P. Purdy, P.-L. Yu, R. W. Peterson, N. S. Kampel, and C. A. Regal, *Phys. Rev. X* **3**, 031012 (2013).
- [23] S. Mookherjea and A. Yariv, *IEEE J. Sel. Top. Quantum Electron.* **8**, 448 (2002).
- [24] B. J. Eggleton, B. Luther-Davies, and K. Richardson, *Nat. Photonics* **5**, 141 (2011).
- [25] J. Dahdah, M. Pilar-Bernal, N. Courjal, G. Ulliac, and F. Baida, *J. Appl. Phys.* **110**, 074318 (2011).
- [26] V. Gurarie, *Phys. Rev. B* **83**, 085426 (2011).
- [27] R. B. Laughlin, *Phys. Rev. Lett.* **50**, 1395 (1983).
- [28] D. C. Tsui, H. L. Stormer, and A. C. Gossard, *Phys. Rev. Lett.* **48**, 1559 (1982).
- [29] H. L. Stormer, D. C. Tsui, and A. C. Gossard, *Rev. Mod. Phys.* **71**, S298 (1999).
- [30] F. Grusdt, M. Höning, and M. Fleischhauer, *Phys. Rev. Lett.* **110**, 260405 (2013).
- [31] Y. Hadad, A. B. Khanikaev, and A. Alù, *Phys. Rev. B* **93**, 155112 (2016).
- [32] See Supplemental Material at <http://link.aps.org/supplemental/10.1103/PhysRevLett.118.197702> for details concerning this point.
- [33] V. E. Manucharyan, J. Koch, L. I. Glazman, and M. H. Devoret, *Science* **326**, 113 (2009).
- [34] A. Ergül, D. Schaeffer, M. Lindblom, D. B. Haviland, J. Lidmar, and J. Johansson, *Phys. Rev. B* **88**, 104501 (2013).
- [35] J. Koch, V. Manucharyan, M. H. Devoret, and L. I. Glazman, *Phys. Rev. Lett.* **103**, 217004 (2009).
- [36] J. Pfeiffer, M. Schuster, A. A. Abdumalikov, and A. V. Ustinov, *Phys. Rev. Lett.* **96**, 034103 (2006).
- [37] D. B. Haviland and P. Delsing, *Phys. Rev. B* **54**, R6857 (1996).
- [38] M. H. Devoret, Quantum Fluctuations, in *Proceedings of the Les Houches Summer School, Session LXIII*, edited by S. Reynard, E. Giacobino, and J. Zinn-Justin (Elsevier, Amsterdam, 1995).
- [39] C. Kane and T. Lubensky, *Nat. Phys.* **10**, 39 (2014).
- [40] S. Shapiro, A. R. Janus, and S. Holly, *Rev. Mod. Phys.* **36**, 223 (1964).
- [41] D.-R. He, W. J. Yeh, and Y. H. Kao, *Phys. Rev. B* **30**, 172 (1984).
- [42] C. A. Hamilton, *Rev. Sci. Instrum.* **71**, 3611 (2000).
- [43] D. R. Hofstadter, *Phys. Rev. B* **14**, 2239 (1976).
- [44] F. D. M. Haldane, *Phys. Rev. Lett.* **61**, 2015 (1988).